

## RESEARCH ARTICLE

10.1002/2016JC012222

## Rip currents and alongshore flows in single channels dredged in the surf zone

Melissa Moulton<sup>1,2</sup> , Steve Elgar<sup>2</sup> , Britt Raubenheimer<sup>2</sup> , John C. Warner<sup>3</sup> , and Nirnimesh Kumar<sup>4</sup> 

## Key Points:

- Rip currents, feeder currents, and meandering alongshore currents were observed in single channels dredged in the surf zone
- The model COAWST reproduces the observed circulation patterns, and is used to investigate dynamics for a wider range of conditions
- A parameter based on breaking-wave-driven setup patterns and alongshore currents predicts offshore-directed flow speeds

## Correspondence to:

M. Moulton,  
mmoulton@apl.uw.edu

## Citation:

Moulton, M., S. Elgar, B. Raubenheimer, J. C. Warner, and N. Kumar (2017), Rip currents and alongshore flows in single channels dredged in the surf zone, *J. Geophys. Res. Oceans*, 122, doi:10.1002/2016JC012222.

Received 7 AUG 2016

Accepted 20 MAR 2017

Accepted article online 23 MAR 2017

<sup>1</sup>Applied Physics Laboratory, University of Washington, Seattle, Washington, USA, <sup>2</sup>Department of Applied Ocean Physics and Engineering, Woods Hole Oceanographic Institution, Woods Hole, Massachusetts, USA, <sup>3</sup>United States Geological Survey, Coastal and Marine Geology Program, Woods Hole, Massachusetts, USA, <sup>4</sup>Department of Civil and Environmental Engineering, University of Washington, Seattle, Washington, USA

**Abstract** To investigate the dynamics of flows near nonuniform bathymetry, single channels (on average 30 m wide and 1.5 m deep) were dredged across the surf zone at five different times, and the subsequent evolution of currents and morphology was observed for a range of wave and tidal conditions. In addition, circulation was simulated with the numerical modeling system COAWST, initialized with the observed incident waves and channel bathymetry, and with an extended set of wave conditions and channel geometries. The simulated flows are consistent with alongshore flows and rip-current circulation patterns observed in the surf zone. Near the offshore-directed flows that develop in the channel, the dominant terms in modeled momentum balances are wave-breaking accelerations, pressure gradients, advection, and the vortex force. The balances vary spatially, and are sensitive to wave conditions and the channel geometry. The observed and modeled maximum offshore-directed flow speeds are correlated with a parameter based on the alongshore gradient in breaking-wave-driven-setup across the nonuniform bathymetry (a function of wave height and angle, water depths in the channel and on the sandbar, and a breaking threshold) and the breaking-wave-driven alongshore flow speed. The offshore-directed flow speed increases with dissipation on the bar and reaches a maximum (when the surf zone is saturated) set by the vertical scale of the bathymetric variability.

## 1. Introduction

Nearshore rip currents and alongshore flows are hazardous to swimmers and are important mechanisms for transporting sediments, pollutants, and larvae across the surf zone and along the shoreline. Rip currents are generated by alongshore variations of breaking-wave-driven setup resulting from local or offshore bathymetric variations, engineered structures, and wave-wave or wave-current interactions [MacMahan *et al.*, 2006; Dalrymple *et al.*, 2011; Castelle *et al.*, 2016; and references therein]. Obliquely incident breaking waves drive alongshore currents, which spatially accelerate (diverge, converge, and meander) as a result of the setup patterns near channels or depressions [Sonu, 1972; Austin *et al.*, 2010; MacMahan *et al.*, 2010; Garnier *et al.*, 2013; Houser *et al.*, 2013; Wilson *et al.*, 2013; Winter *et al.*, 2014; Hansen *et al.*, 2015]. Alongshore currents affect the speed and position of rip-current jets and other offshore-directed flows [Wu and Liu, 1984, 1985; Putrevu *et al.*, 1995; Sancho, 1998; Slinn *et al.*, 2000; Svendsen *et al.*, 2000; Kumar *et al.*, 2011; Wilson *et al.*, 2013].

Numerous field, laboratory, and modeling studies have contributed to the understanding of what controls rip-current presence and speeds [MacMahan *et al.*, 2006; Dalrymple *et al.*, 2011; Castelle *et al.*, 2016; and references therein]. The speed of rip currents generated by local bathymetry varies with alongshore gradients in wave dissipation and setup, which are a function of incident wave properties, tidal elevation, and the geometry of bathymetric features [Bellotti, 2004; Bonneton *et al.*, 2010; Bruneau *et al.*, 2011; Austin *et al.*, 2014]. Rip-current speed has been related to the ratio of offshore wave height to the depth on a sandbar crest (a proxy for dissipation) [Drønen *et al.*, 2002; Haller *et al.*, 2002; MacMahan *et al.*, 2005; Austin *et al.*, 2010; Houser *et al.*, 2013; Winter *et al.*, 2014] and to measures of alongshore bathymetric variability [Castelle *et al.*, 2010; McCarroll *et al.*, 2014], but these empirical relationships do not consider different wave breaking patterns [Winter *et al.*, 2012, 2014; Pitman *et al.*, 2016] or obliquely incident waves.

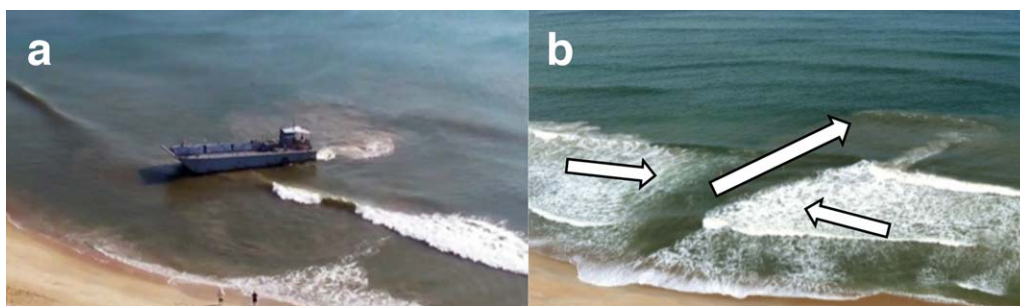


**Figure 1.** Photographs of (a) the landing craft excavating an approximately 2 m deep, 30 m wide (alongshore), and 75 m long (cross-shore) channel across the surf zone, and (b) breaking (white areas on the sides of the channel) and non-breaking (dark areas) waves near the channel. The arrows indicate flow direction. Sediment (brown) and foam (white) carried offshore of the surf zone by the rip current are visible, especially to the right and offshore of the large rip current jet (arrow pointing offshore).

Here, single channels were dredged across the surf zone in Duck, NC at five different times (Figure 1) to investigate the dynamics of rip currents and spatially accelerating (meandering) alongshore flows near non-uniform surfzone bathymetry for a wide range of incident wave conditions, tidal elevations, and channel depths. The evolution of the circulation near the initially 1–2 m deep channels was observed with sensors deployed across the channel thalweg and on the channel sides. The channel bathymetry was surveyed continuously with an array of in situ altimeters [Moulton *et al.*, 2014], allowing for investigation of the sensitivity to bathymetry. The COAWST modeling system [Warner *et al.*, 2008, 2010] is used to investigate the circulation near nonuniform bathymetry for both the observed conditions and for a set of idealized inputs to span a broader range of conditions. Based on modeled momentum balances, a parameterization is developed to provide a simple framework to discuss the dependence of the observed and modeled offshore-directed flow speeds on a wide range of wave, tide, and bathymetric conditions.

## 2. Methods

### 2.1. Dredging Experiments

Field observations were collected near Duck, NC at the US Army Corps of Engineers Field Research Facility (FRF, <http://frf.usace.army.mil/frf.shtml>) between 27 June and 7 August 2012. The propellers on a landing craft (Figure 1a) were used to excavate shore-perpendicular channels in 1–3 m water depth across the terraced or bar-trough morphology (Figure 2). The experiments were performed five times (Figure 2) at different alongshore locations. The FRF coordinates correspond to the approximate cross-shore ( $x$ ) and alongshore ( $y$ ) directions, elevations are relative to NAVD88 (approximately local mean sea level), and times are EDT.

Currents, waves, and tides were measured in and outside of the channels (Figure 2) with colocated pressure sensors (2 Hz), acoustic current meters (2 Hz), and acoustic current profilers (1 min means, 0.1 m bins). In

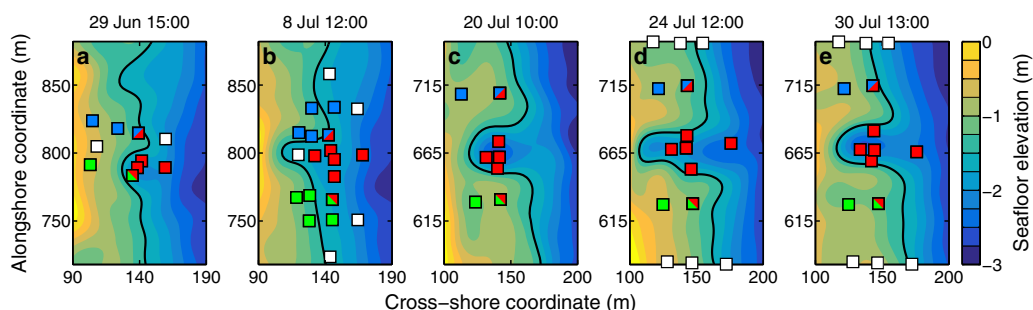


**Figure 2.** Bathymetry (filled color contours every 0.25 m, scale on right, black contour is  $-1.50$  m elevation) of five channels dredged at different times (listed above each plot) in 2012 in Duck, NC as a function of cross-shore ( $x$  axis) and alongshore ( $y$  axis) coordinate. Symbols are locations of colocated current meters and profilers, pressure sensors, and altimeters, with colors indicating locations of observations used to compute time series of flow speeds (Figures 3a and 3b and Figures 4a and 4b). Symbols with two colors were used in two flow speed calculations.

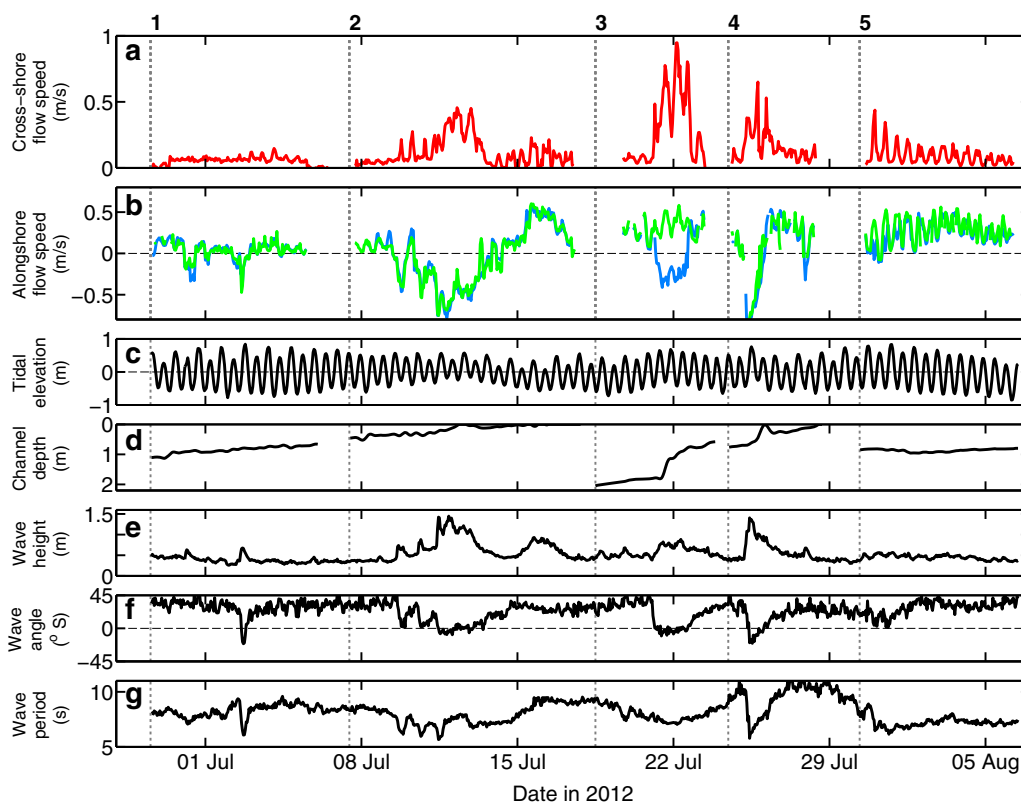


**Figure 3.** Hourly observed (a) maximum offshore-directed flow speed at locations of red symbols in Figure 2, (b) characteristic alongshore flow speeds (positive northward) estimated from observations at locations of blue and green symbols in Figure 2, (c) tidal elevation, (d) channel depth, and incident (e) significant wave height, (f) energy-weighted wave direction (positive is from south of shore normal), and (g) centroidal wave period versus time. The five dashed vertical lines (numbered at the top of Figure 3a) in each plot indicate the times when channels were dredged.

the center of the channel, the depth-averaged velocity was estimated from two profilers (one upward- and one downward-looking) deployed mid-water-column on opposite sides of a pipe, spanning the full water column despite the changing seafloor and tidal elevations. At other locations in the channel, velocity estimates are from downward-looking profilers deployed 1–2 m above the bed, and on the sides of the channel, velocities are estimated using current meters with sample volumes initially  $\sim 0.8$  m above the seafloor. Offshore (incident) wave properties (Figures 3e, 3f, and 3g) were estimated with a colocated pressure gage and current meter in 8.5 m water depth [Hanson *et al.*, 2009], and the tidal elevation (Figure 3c) was measured by a NOAA tide gage in 6 m depth. Significant wave heights ( $H$ ) near the channel and at the offshore gage were computed as four times the standard deviation of sea-surface elevation fluctuations in the frequency band from 0.05 to 0.30 Hz. Centroidal wave periods and energy-weighted wave angles ( $\theta$ ) [Kuik *et al.*, 1988] were computed for the same frequency range. Offshore significant wave heights ranged from 0.3 to 1.5 m, wave incidence angles ranged from  $20^\circ$  north of shore normal to  $45^\circ$  south of shore normal, and centroidal wave periods ranged from 5 to 11 s (Figures 3e, 3f, and 3g). Wave heights ( $H_{br}$ ) and angles ( $\theta_{br}$ ) at breaking were estimated by shoaling and refracting offshore waves to breaking depth using conservation of energy flux, Snell's law, and a depth-limited breaking criterion.

The evolving channel bathymetry was surveyed nearly continuously with in situ altimeters (Figure 2) and daily to weekly (depending on conditions) with a watercraft-based system [Moulton *et al.*, 2014]. One hour altimeter bed-level estimates were smoothed in time (filter timescale = 6 h) to reduce the signal from migrating bed forms [Moulton *et al.*, 2014]. The channel depth at each time (Figure 3d) was estimated as the difference between the depth on the sides (average of altimeter bed-level estimates on north and south sides of channel, Figure 2) and the depth in the channel center (estimated using the altimeter nearest the channel center, Figure 2). The watercraft surveys provide spatially dense estimates of bathymetry at each survey time [Moulton *et al.*, 2014]. The initial bathymetry estimates (Figure 2) for each channel are from the

watercraft survey closest to the time of sensor deployment, within several hours to 2 days after dredging. The bathymetry between survey times was estimated at 3 h intervals using a method that combines observations from watercraft surveys with the hourly bed-level estimates from the in situ altimeters [Moulton *et al.*, 2014]. These estimates of the bathymetry extended  $\sim 160$  m alongshore from the channel center and  $\sim 100$  m cross-shore between the shoreline and  $\sim 3.5$  m depth (Figure 2). Larger-scale bathymetry spanning 1.2 km in the alongshore and from the beach to  $\sim 10$  m depth was measured by an amphibious vehicle before (27 June) and after (10 August) the field experiments. The channels were on average about 30 m wide in the alongshore and 75 m long in the cross-shore (Figure 2), initial channel depths (relative to the average depth on the sides of the channel) were between 0.5 and 2.0 m (Figure 3d), and the water depth on the channel sides ranged from 0.4 to 2.5 m. The artificial channel geometries are similar to observed natural channel bathymetry [Castelle *et al.*, 2016].

## 2.2. Numerical Modeling

Nearshore circulation was simulated using COAWST [Warner *et al.*, 2008, 2010], an open-source modeling system that has skill simulating three-dimensional nearshore and surfzone observations for relatively smooth bathymetry [Kumar *et al.*, 2011, 2012, 2015]. The COAWST simulations are compared with the observations near complex channeled surfzone bathymetry, and are used to investigate momentum balances for a range of incident wave angles.

COAWST couples the wave model SWAN [Booij *et al.*, 1999] with the ocean circulation model ROMS [Haidvogel *et al.*, 2000]. Here, COAWST is run with two-way coupling between ROMS and SWAN. SWAN [Booij *et al.*, 1999] includes shoaling, refraction, and depth-limited wave breaking, and has skill predicting the wave field in complex nearshore environments [van der Westhuysen, 2010; Mulligan *et al.*, 2010; Gorrell *et al.*, 2011; Kumar *et al.*, 2011, 2012, 2015, and many others]. SWAN provides parameters needed to compute wave-related terms in the hydrodynamic model, including Stokes velocities, wave-current interaction, and momentum fluxes from wave breaking. SWAN receives sea-level and circulation fields from the circulation model to determine the effect of water depth and flows on wave propagation. The circulation model ROMS solves the three-dimensional Reynolds-averaged Navier-Stokes equations [Shchepetkin and McWilliams, 2005, 2009; Haidvogel *et al.*, 2008; Warner *et al.*, 2008]. The ROMS module includes wave-current interactions based on the vortex force approach [McWilliams *et al.*, 2004; Smith, 2006] that has been extended to the surf zone [Uchiyama *et al.*, 2010; Warner *et al.*, 2010; Kumar *et al.*, 2011, 2012], a scheme for wave-induced mixing via a surface boundary condition [Feddersen and Trowbridge, 2005], the vertical structure of depth-limited wave-dissipation induced acceleration, and bottom streaming effects [Henderson *et al.*, 2004].

ROMS and SWAN are run on the same 2 m horizontal grid, spanning 4 km in the alongshore centered on a single channel, and from the shoreline to 9 m depth. The results are not sensitive to doubling or halving the grid resolution. ROMS is run with 10 vertical layers, and both models are run with a time step of 0.5 s with a coupling interval of 15 s. Each simulation is run for a period of 3 h with constant bathymetry and wave forcing, allowing the flows to spinup fully. The average of the final hour of the 3 h run is used for analysis. For each run, depth-averaged Eulerian mean flows are used to estimate the maximum offshore-directed flow and the characteristic alongshore flows.

SWAN solves the wave action balance for a frequency-directional spectrum with 180  $2^\circ$  wide directional bands, and 21 frequency bands logarithmically spaced from 0.04 to 1.00 Hz. Depth-limited wave breaking [Battjes and Janssen, 1978; Thornton and Guza, 1983; Battjes and Stive, 1985; Raubenheimer *et al.*, 1996; Apotos *et al.*, 2008] is modeled using a free parameter that controls the maximum ratio of wave height to water depth for a distribution of wave heights, and that is set to the default value of  $\gamma_{BJ} = 0.73$  [Battjes and Janssen, 1978]. The sensitivity of the rip-current speed to  $\gamma_{BJ}$  was approximately linear.

Although Coriolis, tidal, wind, and buoyancy forcing can influence inner shelf flows outside the surf zone [Lentz *et al.*, 1999], these terms were not included for the ROMS simulations of wave-driven well-mixed surfzone flows considered here. The bottom stress is computed with a quadratic drag law with a standard value of the drag coefficient  $C_d = 0.0033$  [Feddersen *et al.*, 2003], and the horizontal viscosity is set to 0.05  $\text{m}^2/\text{s}$  to account for subgrid scale mixing. Consistent with previous studies, the flows are not sensitive to the drag formulation [Ganju and Sherwood, 2010] or viscosity. A General Length Scale (GLS,  $k-\epsilon$ ) [Warner *et al.*, 2005] turbulence scheme is used. The effects of wave rollers [Reniers *et al.*, 2004] are parameterized assuming that 50% ( $\alpha_r = 0.5$ ) of the wave energy dissipation goes to the roller (the rest goes to local dissipation) [Tajima

and Madsen, 2006; Kumar *et al.*, 2012]. The rip-current speed varies by up to 15% for changes in  $\alpha_r$  from 0 to 1. The boundary conditions are closed at the shoreline and open at the offshore, north, and south boundaries. At the offshore boundary, a Flather radiation condition is applied for sea level and barotropic flows [Flather, 1976; Chapman, 1985], and a gradient condition is used for baroclinic velocities [Haidvogel *et al.*, 2008]. Gradient boundary conditions are applied at the other open boundaries.

### 2.3. Flow Speed Estimates

The flow patterns near the channels are spatially complex and sensitive to the bathymetry and wave properties. The strongest cross-shore flows sometimes were shifted from the channel center to or beyond the channel edges in the direction of a breaking-wave-driven alongshore flow, and alongshore flows were maximum at different cross-shore positions and sometimes changed sign in the cross shore. Thus, characteristic flow speeds are defined within regions rather than at specific positions.

The maximum observed offshore-directed flow speed is defined as the maximum hour-averaged offshore-directed cross-shore component of flows measured at sensors in and near the edges of the channel (red symbols in Figure 2). The maximum-modeled offshore-directed flow speed is defined as the maximum cross-shore component of flows in a region spanning 40 m alongshore (centered on the rip channel) and extending from near the shoreline to the offshore edge of the sandbar (average depth  $\sim 2$  m).

The maximum alongshore flow toward the channel, maximum alongshore flow away from the channel, and average alongshore flow were computed for observations on the north and south sides of the channel (blue and green sensor locations in Figure 2), and for simulations in the regions extending from the channel center to 30 m north or south of the channel center and from the shoreline to the bar crest. The characteristic alongshore flow on each side of the channel is defined as the strongest alongshore flow toward the channel if flows toward the channel exceed 0.1 m/s and (for the simulations) extend over a region  $> 100$  m<sup>2</sup>. These requirements reduced the possibility of classifying weak and spatially limited flows (e.g., small recirculation cells) as feeder currents. If the maximum observed or modeled flow toward the channel does not exceed the thresholds, the characteristic flow is defined as the maximum flow in the direction of the mean alongshore current near the channel.

## 3. Results

### 3.1. Observed and Modeled Flows in Dredged Channels

For the five channel-dredging experiments, offshore-directed flow speeds increased for larger wave heights (Figure 3e), more normally incident wave directions (Figure 3f), and lower tidal elevation (Figure 3c), consistent with previous field studies and with rip-current rescue statistics [Dusek and Seim, 2013]. Obliquely incident waves produced alongshore flows across the channel with offshore-directed flows (Figures 3a, 3b, and 3f) that often were strongest at sensor locations on the downstream side of the channel. The third channel-dredging experiment (Figures 2c, 3, and 4) included a wide range of wave conditions and channel depths, and transitions between alongshore flows ( $\sim 0.3$  m/s) and a tidally modulated rip-current circulation pattern including feeder currents and a strong (up to nearly 1 m/s) jet, and thus was chosen for detailed investigation.

The model was run with the observed hour-averaged wave forcing every 3 h during the third channel dredging experiment, from 19 July 18:00 to 23 July 09:00 (Figure 4), excluding several times during low tide when many sensors were dry (a total of 27 simulations). The 3 h interval between simulations resolves the temporal changes in the wave forcing and tidal elevation. Near the channels ( $\pm 80$  m alongshore from the center, from the shoreline to  $\sim 3.5$  m depth) the model bathymetry for each time was updated to be consistent with observations from the watercraft surveys and the altimeters [Moulton *et al.*, 2014]. Including differences in the shoreline position in the model bathymetry on the north and south sides of the domain with steady wave forcing led to large-scale alongshore pressure gradients that impacted the circulation at the channel. For the results presented here, the model bathymetry is alongshore uniform away from the channel, with depths at each cross-shore location equal to the average of the June and August large-scale surveys. The uniform bathymetry isolates the effects of the channel on the circulation, but introduces errors from ignoring spatial variability offshore and alongshore of the channel.

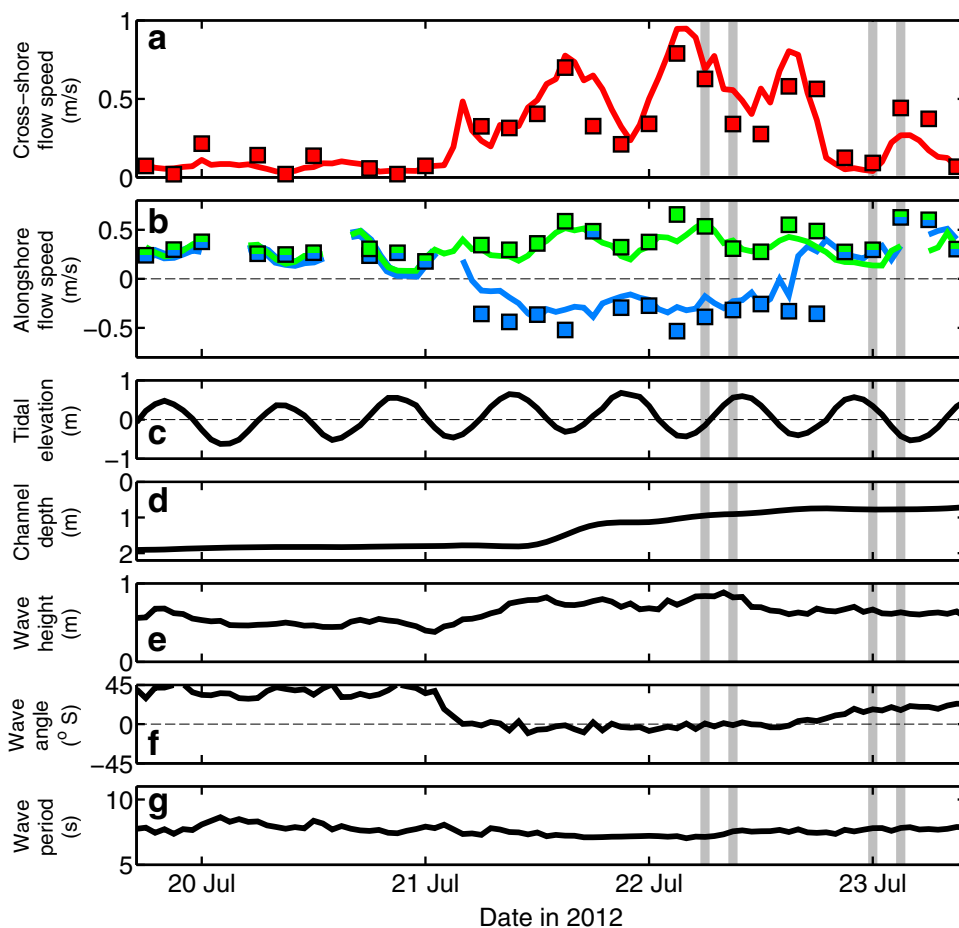


**Figure 4.** (a) Maximum observed (curve) and modeled (squares) offshore-directed flow speed in the channel (red symbols in Figure 2c), (b) characteristic observed (curves) and modeled (squares) alongshore flow speeds (positive is northward) on north and south sides of the channel (blue and green symbols in Figure 2c), (c) tidal elevation, (d) channel depth, and incident (e) significant wave height, (f) energy-weighted wave direction (positive is from south of shore normal), and (g) centroidal wave period versus date in 2012 for the third channel dredging experiment (Figure 3). In Figure 4b, at times when the characteristic modeled speeds on the sides of the channel are similar to each other (difference  $< 0.05$  m/s), a single symbol with both blue and green color is shown. The four gray bars indicate the times shown in Figure 5.

Observed and modeled wave heights (not shown) are similar (root mean square error,  $rmse = \sim 0.1$  m, and  $|bias| < 0.1$  m), with smallest error and bias at locations on the shoals where waves often were depth-limited, and slightly larger errors for sensors in the channel. The sign of the modeled wave angle (averaged over the sensor locations near the channel) is consistent with the averaged observed wave angle near the channel, changing from southerly to northerly on 21 July and back to southerly by 23 July. The values and spatial patterns of the observed and modeled wave angles (not shown) differed near the channel ( $7^\circ < rmse < 18^\circ$ ), likely as a result of inaccuracies in the model bathymetry, errors in compasses ( $\sim 5^\circ$ ) and estimates of wave angles, and errors in the modeled refraction on the rip jet and channel bathymetry, which changes rapidly over a wavelength.

The maximum modeled (symbols in Figure 4a, black arrows in Figure 5) and observed (curve in Figure 4a, white arrows in Figure 5) offshore-directed flow speeds are similar (normalized (by the range of the observations) root-mean-square error,  $normse = 0.15$ ), with weak flows on 20 July, followed by a tidally modulated rip current. The modeled alongshore components of the flows on the north and south sides of the channel (Figure 4b, symbols) also are similar to the observed flows ( $normse = 0.23$  on the north side, and  $0.26$  on the south side), with an alongshore-current pattern (flows on the north and south sides of the channel both towards the north) on 20 and 23 July when the wave direction is most oblique (Figures 5c and 5d), and with feeder current patterns (alongshore flows converging toward the channel) on 21 and 22 July when the wave direction is closer to shore-normal (Figures 5a and 5b).

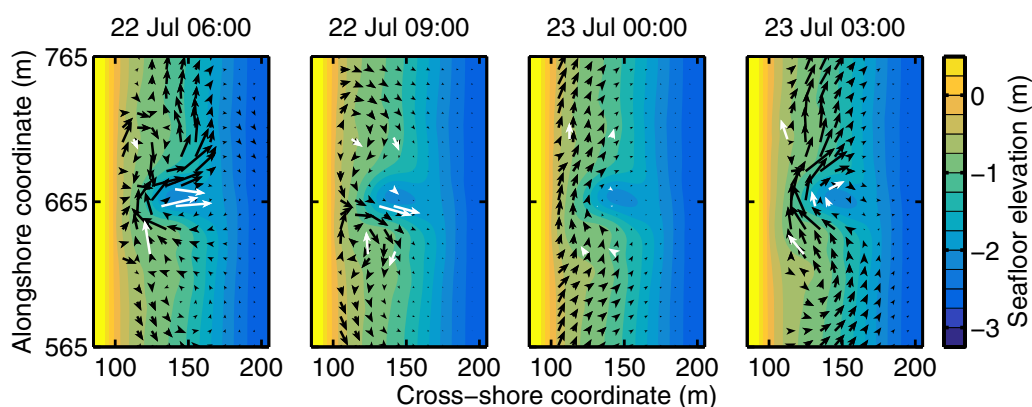


**Figure 5.** Water depth (filled color contours every 0.25 m, scale on the right, black contours are 0 and  $-1.50$  m seafloor elevation) and observed (white arrows) and modeled (black arrows, plotted every 10 m) 1 h-averaged flows [scale in (a)] as a function of cross-shore and alongshore coordinate at four times (listed above each plot). The current meters on the sides of the channel at cross-shore distance  $\sim 140$  m were dry at low tide, and thus observations from those sensors are not shown in (a) or (d).

Observed and modeled rip-current jets (Figures 5a and 5b) sometimes are located on the sides of the channel. Observed jets are located in the middle of the channel more often than modeled jets, and variability in the hour-averaged jet position is larger in the simulations than in the observations. These results are consistent with previous studies in which the position of modeled rip-current jets is sensitive to small asymmetries in the model forcing [Haas *et al.*, 2003; Haas and Warner, 2009]. Observed and modeled alongshore flows sometimes change sign in the cross-shore as part of a circulation cell (Figure 5b, south side of channel). When alongshore flows are present as a result of oblique wave forcing, modeled and observed flows are onshore-directed on the upstream side of the channel and offshore-directed on the downstream side of the channel, and the strength of the meanders is modulated by the tidal elevation (Figures 5c and 5d). At some times, the strongest modeled offshore-directed flow is downstream of the northernmost sensor in the channel (Figures 5c and 5d), suggesting that the sparsely spaced observations sometimes may not have included the strongest flows in the circulation patterns.

### 3.2. Dynamics of Flows in Channels

The time-averaged wave forcing associated with breaking drives an increase in the mean water level (setup) near the shoreline [Longuet-Higgins and Stewart, 1964], and drives alongshore currents in the case of obliquely incident waves [Longuet-Higgins, 1970]. The initial cross-shore position of wave breaking, estimated as the location where the ratio of wave height to the water depth reaches a threshold ( $H_{br}/h = \gamma = 0.73$ ), varies spatially, primarily as a function of bathymetry (Figures 6a–6d, dashed gray curves). At low tide during the third channel dredging experiment, waves break in the shallow water on the sides of the channel, but not in the deeper channel, leading to a strong alongshore difference in wave dissipation and setup ( $\sim 0.04$  m) across the channel (Figures 6a and 6d). At high tide (Figures 6b and 6c), dissipation is weak on the bar and maximum near the shoreline, with a small ( $\sim 0.01$  m) alongshore difference in the sea level near the shoreline resulting from wave refraction on the channel bathymetry.

The modeled dissipation and sea-level patterns (Figure 6) are similar for cases at low tide (e.g., Figures 6a and 6d) and for cases at high tide (e.g., Figures 6b and 6c) despite different wave angles, but the flow patterns differ substantially (compare Figure 5a with 5d, and Figure 5b with 5c). Thus, although the wave angle has a small impact on the modeled wave dissipation and sea-level patterns, it has a large impact on the circulation pattern. Alongshore sea-level differences led to rip-current circulation patterns when waves were shore-normal (Figures 5a and 5b) and to spatial accelerations of the alongshore flow when waves were oblique (Figures 5c and 5d), with the strength of the rip jets or flow meanders controlled primarily by the strength of alongshore gradients in dissipation and sea-level (Figures 5 and 6).

The depth-averaged cross-shore and alongshore momentum balances using the vortex-force approach are [Kumar *et al.*, 2012]:

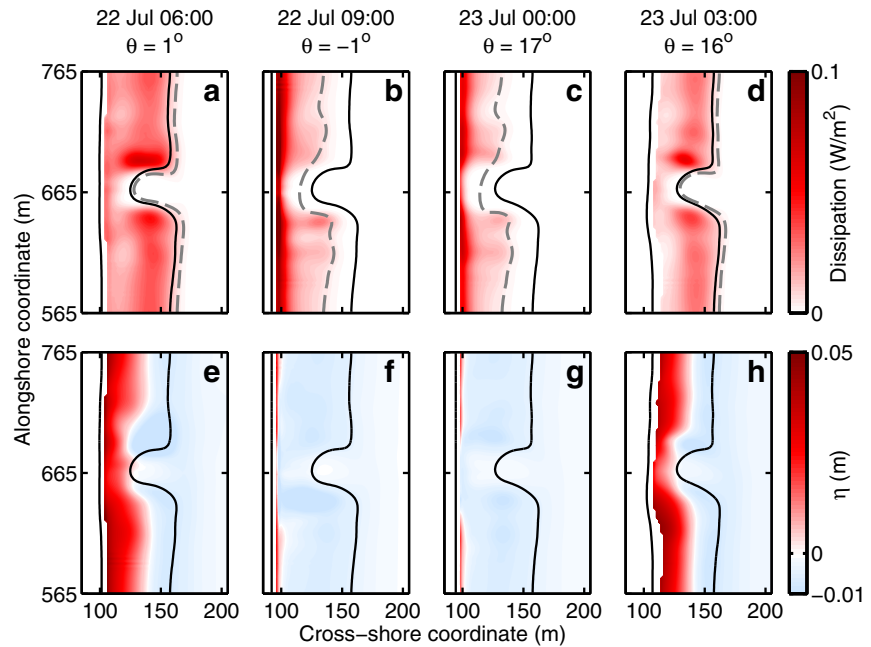


**Figure 6.** Filled color contours (scales at right) of modeled (a–d) wave dissipation and (e–h) sea level as a function of cross-shore and alongshore coordinate at four times, with black contours at 0 and  $-1.25$  m seafloor elevation, and (top row) dashed gray contours at the approximate location where waves break ( $H_{br}/h = \gamma = 0.73$ ). Times and incident wave angles relative to shore normal are listed at the top of each plot.

$$\underbrace{\frac{\partial \bar{u}}{\partial t}}_{\text{x-acceleration}} + \underbrace{\left[ \frac{\partial \bar{u}v}{\partial x} + \frac{\partial \bar{u}u}{\partial y} + \bar{u} \left( \frac{\partial \bar{u}^{St}}{\partial x} + \frac{\partial \bar{v}^{St}}{\partial y} \right) \right]}_{\text{x-advection}} - \underbrace{\bar{v}^{St} \left( \frac{\partial \bar{v}}{\partial x} - \frac{\partial \bar{u}}{\partial y} \right)}_{\text{x-vortex force}} = - \underbrace{\frac{\partial \bar{\phi}}{\partial x}}_{\text{x-pressure gradient}} - \underbrace{\frac{\tau_{bx}}{\rho h}}_{\text{x-bottom stress}} + \underbrace{\bar{F}^{wx}}_{\text{x-wave breaking}} \quad (1)$$

$$\underbrace{\frac{\partial \bar{v}}{\partial t}}_{\text{y-acceleration}} + \underbrace{\left[ \frac{\partial \bar{u}v}{\partial x} + \frac{\partial \bar{v}v}{\partial y} + \bar{v} \left( \frac{\partial \bar{u}^{St}}{\partial x} + \frac{\partial \bar{v}^{St}}{\partial y} \right) \right]}_{\text{y-advection}} + \underbrace{\bar{u}^{St} \left( \frac{\partial \bar{v}}{\partial x} - \frac{\partial \bar{u}}{\partial y} \right)}_{\text{y-vortex force}} = - \underbrace{\frac{\partial \bar{\phi}}{\partial y}}_{\text{y-pressure gradient}} - \underbrace{\frac{\tau_{by}}{\rho h}}_{\text{y-bottom stress}} + \underbrace{\bar{F}^{wy}}_{\text{y-wave breaking}} \quad (2)$$

where  $t$  is time,  $u$  and  $u^{St}$  and  $v$  and  $v^{St}$  are Eulerian mean and Stokes velocities, respectively, in the cross-shore ( $x$ ) and alongshore ( $y$ ) directions,  $\phi$  is the geopotential function,  $F^w$  is the momentum flux from nonconservative wave terms,  $\tau_b$  is the bottom stress,  $\rho$  is the water density,  $h$  is the water depth, and overbars denote depth averages. The terms (left to right) are local acceleration, horizontal advection, the vortex force, pressure gradients, bottom stress, and nonconservative wave forcing (including dissipation from depth-limited wave breaking and wave roller contributions). The dynamics are not sensitive to horizontal mixing (not shown), which was at least an order of magnitude smaller than the dominant terms.

Momentum balances for the observed dredged channel bathymetry and wave conditions are investigated using the set of 27 model simulations forced with observed conditions from 19 July 18:00 to 23 July 09:00. Near the channels, the dominant terms in depth-averaged momentum balances are advection, the vortex force, pressure gradients, and wave-breaking accelerations, consistent with studies using idealized channel bathymetry [Kumar *et al.*, 2011] and studies of rip currents controlled by offshore bathymetry [Long and Özkan-Haller, 2005, 2016; Hansen *et al.*, 2015]. Far from the channel (not shown), the modeled alongshore balance is between the bottom stress, wave-breaking accelerations, advection, and the vortex force, all of which are one to two orders of magnitude smaller than the dominant terms near the channel, similar to results from previous COAWST simulations with idealized bathymetry [Kumar *et al.*, 2012].

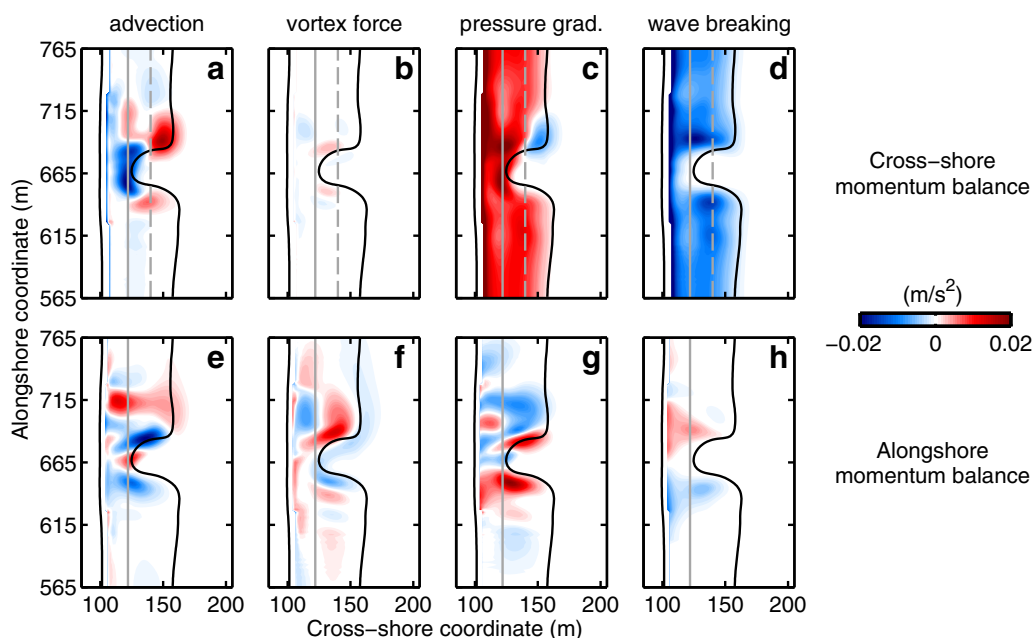


**Figure 7.** Filled color contours of dominant terms (labeled at top) in modeled depth-averaged cross-shore (top row) and alongshore (bottom row) momentum balances for observed conditions on 22 July 06:00. Black contours are 0 and  $-1.25$  m seafloor elevation. Advection and vortex force terms are plotted with opposite sign, equivalent to moving them to the right side of equations (1) and (2). Gray solid and dashed vertical lines are the positions of transects shown in Figure 8.

In modeled cross-shore momentum balances for a wide range of conditions, wave-breaking accelerations (Figure 7d, dashed green curves in Figures 8a and 8b) primarily are balanced by pressure gradients (wave setup) (Figure 7c, dashed red curve in Figures 8a and 8b) on the channel sides. The mean sea level (Figures 6e and 6f) and cross-shore pressure gradient (dashed red curve in Figures 8a and 8b) decrease toward the channel center as a result of the rip-current circulation pattern. In a narrow region on the edges of the channel ( $\sim 20$  m north and south of the gray shaded region in Figures 8a and 8b), wave-breaking accelerations enhanced by refraction are balanced by pressure gradients and onshore accelerations (blue curves in Figures 8a and 8b) of the flow (Figures 5a and 5d). Near the onshore edge of the channel (solid gray line in Figures 7a–7d), a large cross-shore pressure gradient (solid red curve in Figure 8a) resulting from converging alongshore flows drives advective accelerations (solid blue curve in Figure 8a), representing the spatial accelerations of the rip-current jet.

Near the channels, modeled alongshore momentum balances for obliquely incident waves (e.g., 23 July 03:00, Figures 8b, 8d, and 8f) are similar to balances for shore-normal waves (e.g., 22 July 06:00, Figures 8a, 8c, and 8e), with the sum of pressure gradients and wave-breaking accelerations (orange curve in Figure 8f) balancing the sum of advection and the vortex force (gray curve in Figure 8f). There are regions with negative forcing on the north side of the channel (region 1, Figures 8e and 8f) and positive forcing on the south side of the channel (region 4, Figures 8e and 8f), and the largest contribution to the forcing is from the pressure gradient (red curve in Figures 8c and 8d). In between those regions, the forcing changes sign (regions 2 and 3, Figures 8e and 8f), and there is a zero crossing near where flows turn seaward (Figures 5a and 5d). This pattern was consistent for the wide range of modeled conditions (not shown).

Unlike in inlets [Olabarrieta *et al.*, 2014] and inner shelf environments, the vortex force is a significant term in the momentum balances near surfzone channels. For waves opposing an offshore-directed jet, the sheared current causes waves to refract toward the jet, and thus the waves exert a reciprocal force (vortex force) on the currents that is directed away from the jet [Smith, 2006]. The vortex force term (Figure 7f and back curve in Figures 8c and 8d) is largest where the flow vorticity is largest and changes sign with the flow vorticity (equation (2)), with opposite sign on either side of the jet or offshore-directed flow maximum.

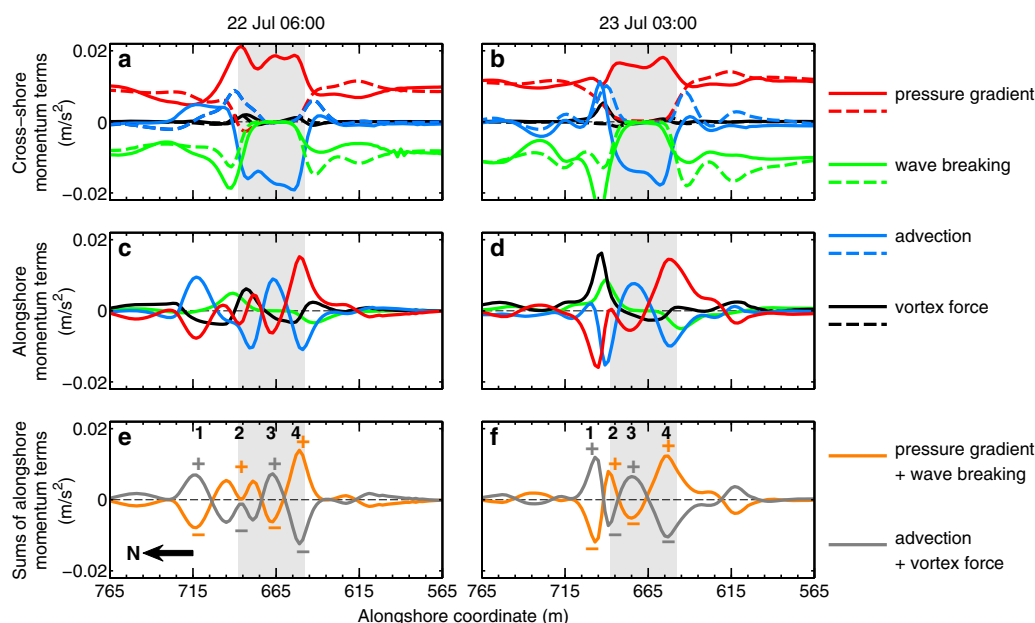


**Figure 8.** (a and b) Depth-averaged modeled cross-shore momentum balance terms (at cross-shore positions of solid and dashed gray lines in Figure 7), (c and d) alongshore momentum terms (at position of solid gray lines in Figure 7), and (e and f) sums of alongshore momentum terms (positive and negative regions labeled and numbered) near the channel (gray shading) versus alongshore coordinate for observed conditions (Figure 4) on (a, c, e) 22 July 06:00 and (b, d, f) 23 July 03:00. Advection and vortex force terms are plotted with opposite sign, equivalent to moving them to the right side of equations (1) and (2). The alongshore coordinate is plotted with north on the left, from the perspective of an observer on the beach looking offshore.

Alongshore wave-breaking accelerations are small relative to other alongshore momentum balance terms near the channel, except in a small region near the channel edges where wave-breaking accelerations are directed away from the channel (Figure 7h, green curves in Figures 8c and 8d) as a result of refraction on the channel bathymetry. These accelerations are balanced partially by pressure gradients enhanced by focusing of wave breaking on the channel sides, suggesting that wave refraction has a small net effect on the size of feeder currents, consistent with previous studies [Kumar *et al.*, 2011].

Although the bottom stress and oblique wave forcing are small compared with the other terms near the channel, the northward obliquely incident breaking-wave-driven alongshore flow (Figure 5d, 23 July 03:00) leads to differences in the momentum balance and circulation near the channel relative to cases with normally incident waves. For example, for obliquely incident waves, the location of the zero-crossing in the summed balance (between regions 2 and 3 in Figures 8e and 8f) where flows turn seaward (Figures 5a and 5d) is shifted in the direction of the alongshore current.

## 4. Discussion

### 4.1. Parameterization of the Maximum Offshore-Directed Flow Speed

A parameterization based on the modeled momentum balances is developed to provide a simpler framework for assessing the dependence of the offshore-directed flow speed on changes in wave conditions, bathymetry, and tidal elevation. Sea-level patterns and flow speeds in multiple closely spaced channels (less than  $\sim 5$  channel-widths apart) may deviate from those considered here [Svendson *et al.*, 2000].

Based on the assumptions that pressure gradients and wave-breaking accelerations are the dominant terms in the cross-shore momentum balance [Longuet-Higgins and Stewart, 1964; Lentz and Raubenheimer, 1999; Raubenheimer *et al.*, 2001], bottom stress and wave rollers do not have a first-order impact on the sea-level profile [Apotsos *et al.*, 2007], gradients in sea level are small compared with the water depth, and wave height is depth-limited at breaking ( $H_{br} = \gamma h$ ), the cross-shore gradient in sea level  $\eta(x)$  is given by [Bowen *et al.*, 1968]:

$$\frac{\partial \eta}{\partial x} \approx \begin{cases} 0 & \text{if } H_{br} < \gamma h \text{ (non-breaking)} \\ -\frac{1}{16} \gamma^2 \left( \cos^2 \theta_{br} + \frac{1}{2} \right) \frac{\partial h}{\partial x} & \text{if } H_{br} = \gamma h \text{ (breaking)} \end{cases} \quad (3)$$

This approximation ignores the setdown of the water level during wave shoaling, the effects of wave refraction after breaking (the wave angle is approximated as constant and equal to the wave angle at breaking  $\theta_{br}$ ), wave-current interaction, and the impacts of circulation on the sea-level pattern. Equation (3) can be solved for  $\eta(x)$  on the channel sides and in the channel by estimating the wave angle and height at breaking from offshore properties and integrating over bathymetric profiles. The maximum of the difference between the profiles on the shallow sides  $\eta_{bar}(x)$  and in the deep channel  $\eta_{chan}(x)$  is chosen as a scale for the alongshore sea-level difference that drives feeder currents, given by  $\Delta\eta_y \approx \max(\eta_{bar}(x) - \eta_{chan}(x))$ .

If waves propagating over an alongshore-uniform sandbar interrupted by a single channel are small relative to the depth on the bar, they break in a region near the shoreline where the beach is alongshore uniform ("shore-break"), and there is no alongshore variability in the setup and  $\Delta\eta_y \approx 0$ . If waves break on the shallow sides, but not in the deeper channel ("bar-break"), the maximum  $\Delta\eta_y$  often occurs near the cross-shore position of the bar crest. The maximum setup on the sides of the channel scales with the difference between the depth at breaking ( $h_{br} = H_{br}/\gamma$ ) and the depth on the bar crest ( $h_{bar}$ ). Ignoring setdown, the setup in the middle of the channel is approximately zero, and the alongshore sea-level difference  $\Delta\eta_y$  scales with  $(H_{br}/\gamma - h_{bar})$ . If waves are large enough to break offshore of the alongshore variability (the surf zone is "saturated"), waves are depth limited in the channel and on the bar, and the maximum alongshore sea-level difference is set by the difference in depths in the channel and on the bar ( $h_{chan} - h_{bar}$ ). Thus, alongshore sea-level differences driving feeder currents are approximated by:

$$\Delta\eta_y \approx \begin{cases} 0 & \text{if } H_{br} < \gamma h_{bar} \text{ (shore-break)} \\ \frac{1}{16} \gamma^2 \left( \cos^2 \theta_{br} + \frac{1}{2} \right) (H_{br}/\gamma - h_{bar}) & \text{if } \gamma h_{bar} < H_{br} < \gamma h_{chan} \text{ (bar-break)} \\ \frac{1}{16} \gamma^2 \left( \cos^2 \theta_{br} + \frac{1}{2} \right) (h_{chan} - h_{bar}) & \text{if } H_{br} > \gamma h_{chan} \text{ (saturated)} \end{cases} \quad (4)$$

Although bottom stress may be important for wider or shallower channels, for the channels considered here the ratio of the bottom stress term to the advection term is small ( $C_D L_y / \Delta h \sim 0.1$ , where  $L_y$  and  $\Delta h$  are alongshore and vertical bathymetric length scales). Thus, assuming a balance of pressure gradients and advection along a streamline, feeder currents driven by the alongshore sea-level difference  $\Delta\eta_y$  can be approximated using the Bernoulli relationship  $\nabla \left( \frac{1}{2} |\vec{v}|^2 + g\eta \right) \approx 0$ , where  $g$  is the gravitational acceleration. The change in speed of the alongshore flow far from the channel ( $V_A$ ) to the edge of the channel ( $V_C$ ) is obtained approximately by solving  $(V_C^2 - V_A^2) \approx 2g\Delta\eta_y$  with  $\Delta V = V_C - V_A$ , yielding  $\Delta V = \left( 2g\Delta\eta_y - V_A^2 \right)^{1/2} - V_A$ , which also can be expressed as  $\Delta V = (2g\Delta\eta_y)^{1/2} [(1+a^2)^{1/2} - a]$ , where  $a = V_A / \sqrt{2g\Delta\eta_y}$ . The alongshore flow far from the channel is expected to be equal to the breaking-wave-driven alongshore flow on a uniform beach with no channel. Previous studies [Bellotti, 2004; Kumar et al., 2011; Garnier et al., 2013] and the observations and simulations presented here suggest that the maximum offshore-directed flow near the channel ( $U$ ) increases with the alongshore difference in the alongshore velocity ( $\Delta V$ ). Thus, assuming  $U \propto \Delta V$ ,

$$U \approx \sqrt{2g\Delta\eta_y} F_V \quad (5)$$

where  $F_V$  represents the effects of the inertia of the alongshore current, or the additional work needed to change the velocity of a faster flow, with

$$F_V \approx \left[ (1 + (\beta a)^2)^{1/2} - \beta a \right] \quad (6)$$

where  $a = V_A / \sqrt{2g\Delta\eta_y}$ , the ratio of the breaking-wave-driven alongshore flow  $V_A$  to the expected size of flows driven by alongshore gradients in setup  $\sqrt{2g\Delta\eta_y}$ , and the constant  $\beta$  controls the sensitivity to the alongshore flow ( $0 < \beta < 1$ ), which may weaken across the channel [Winter, 2012]. The alongshore-current speed  $V_A$  can be estimated [Bowen, 1969; Longuet-Higgins, 1970; Thornton, 1970; Thornton and Guza, 1986; Guza et al., 1986; Feddersen et al., 1998; and many others] using an alongshore momentum balance

(equation (2)) between wave-breaking accelerations and bottom stress. Here, the alongshore-current speed far from the channel was estimated using a quadratic bottom stress formulation, leading to  $V_A = \frac{\sqrt{5}}{4} C_D^{-1/2} \alpha^{1/2} \gamma^{3/4} (g H_{br,v} \sin \theta_{br})^{1/2}$ , where  $\alpha$  is the average beach slope. The adjusted breaking wave height,  $H_{br,v}$  is the wave height at breaking  $H_{br}$  with an upper bound equal to the depth-limited breaking wave height on the bar crest [ $\max(H_{br,v}) = \gamma h_{bar}$ ] such that  $V_A$  is the alongshore-flow speed at or onshore of the bar crest. Stronger alongshore flows generated offshore of the bathymetric variability for  $H_{br} > \gamma h_{bar}$  are not expected to affect  $U$ . Results are similar without the upper bound.

For saturated wave conditions, the sea-level difference (equation (4)) and offshore-directed flow speed (equation (5)) reach maximum values set by the bathymetry (neglecting the effects of the alongshore flow, i.e.,  $F_V = 1$ ):

$$\Delta \eta_{y,sat} \approx \frac{1}{16} \gamma^2 \left( \cos^2 \theta_{br} + \frac{1}{2} \right) \Delta h \quad (7)$$

$$U_{sat} \approx \sqrt{2g \Delta \eta_{y,sat}} \quad (8)$$

where  $\Delta h = (h_{chan} - h_{bar})$  is the vertical scale of the alongshore bathymetric variability.

#### 4.2. Controls on the Offshore-Directed Flow Speed

To test the parameterizations for the sea-level difference and offshore-directed flow speed for a range of wave conditions, tidal elevations, and channel depths, 150 idealized model runs were performed. Similar to the model runs with observed conditions, the domain extends 4 km in the alongshore centered on a single channel, and from the shoreline to approximately 9 m water depth. Incident waves have a JONSWAP spectral shape [Hasselmann *et al.*, 1973] with constant spectral width ( $\gamma_{JS} = 1$ ), peak period ( $T = 7$  s), and directional spread ( $36^\circ$ ) based on the average values from fits to observed spectra. The offshore wave height  $H$  varies from 0.05 to 2.00 m and the wave angle  $\theta$  varies from  $0$  to  $45^\circ$ . The beach bathymetry is planar (slope = 0.03), except for a 1 m high, 64 m wide (four times the standard deviation) Gaussian-shaped sandbar located between 30 and 90 m from the shoreline (depending on tidal elevation, beach slope, and bar height), consistent with bathymetry observed in the summer in Duck, NC [Voulgaris *et al.*, 2011]. The sandbar is interrupted by a 40 m wide Gaussian channel. The difference in water depth between the channel center and the bar crest,  $\Delta h$ , varies between 0.1 and 1.0 m, similar to the geometry of the dredged channels. The results are not sensitive to doubling or halving the channel or bar widths, consistent with previous laboratory and numerical studies [Kennedy *et al.*, 2008; Winter *et al.*, 2012, 2014]. The tidal elevation ( $h_{bar}$ , the depth on the bar crest) varies from 0.2 to 2.0 m. The 150 runs include 36 runs with all combinations of a set of four parameter values ( $H = 0.25, 0.75, \text{ and } 1.00$  m;  $\theta = 0^\circ, 10^\circ, \text{ and } 30^\circ$ ;  $\Delta h = 0.25 \text{ and } 1.00$  m; and  $h_{bar} = 0.5 \text{ and } 1.0$  m) and runs with wider ranges and finer variations of the four parameters.

Simulations with shore normal waves, fixed tidal elevation (0.5 m depth on bar crest), fixed channel depth (1 m depth relative to bar crest), and a range of wave heights that span the breaking regimes are compared with the parameterization. For waves that are small relative to the bar crest elevation ( $H_{br} < \gamma h_{bar}$ ), the waves break close to the shoreline, and the sea-level difference  $\Delta \eta_y$  in the alongshore is near zero (shore-break, equation (4), Figure 9a). The parameterized dissipation (section 4.1) uses the bulk significant wave height and angle, which results in zero sea-level difference, whereas modeled dissipation [Battjes and Janssen, 1978] is based on a distribution of wave heights and there is some dissipation (and thus a small setup gradient) even when  $H_{br} < \gamma h_{bar}$ . In addition, the parameterization ignores refraction, which leads to focusing of wave energy and higher sea level near the shoreline on the sides of the channel, similar to wave focusing by offshore bathymetry [Long and Özkan-Haller, 2005, 2016; List *et al.*, 2009]. Wave refraction also leads to wave-breaking accelerations directed away from the channel, which partially compensate the pressure gradients that result from wave focusing, resulting in a weak net effect on offshore-directed flows (Figure 9b, shore-break).

For moderate waves ( $\gamma h_{bar} < H_{br} < \gamma h_{chan}$ ) that break on the bar, but not in the channel, the alongshore sea-level difference increases with increasing wave height (bar-break, equation (4), Figure 9a). The offshore-directed flow speed also increases with wave height (Figure 9b), consistent with the parameterization

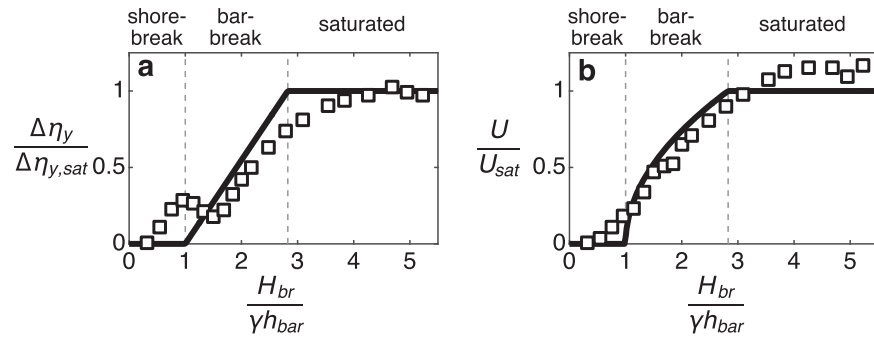


**Figure 9.** Parameterized (equations (4) and (5), curves) and simulated (squares) normalized (by their parameterized saturated values (equations (7) and (8))) (a) alongshore sea-level difference  $\Delta\eta_y/\Delta\eta_{y,sat}$  and (b) offshore-directed flow speed  $U/U_{sat}$  versus parameterized  $H_{br}/\gamma h_{bar}$  for model runs with shore-normal waves with a range of wave heights and fixed bathymetry and tidal elevation.

(equation (5),  $F_V = 1$  for shore-normal waves). For large waves ( $H_{br} > \gamma h_{chan}$ ) that are depth-limited in the channel and on the shallow sides, the alongshore sea-level difference does not increase with wave height (saturated, equation (7), Figure 9a). The parameterized saturated sea-level difference ( $\Delta\eta_{sat} = 0.048$  m) is similar to the modeled value ( $\Delta\eta_{sat,mod} = 0.046$  m). Consistent with the parameterization (equation (8)), the simulated  $U$  reaches a maximum value (Figure 9b), although the parameterized saturated flow speed ( $U_{sat} = 0.97$  m/s) is about 10% smaller than the modeled value ( $U_{sat,mod} = 1.08$  m/s). Similarly, for model simulations with fixed wave height and varying tidal elevation (varying depth on the bar,  $h_{bar}$ ) (not shown) or different channel depths ( $\Delta h$ ) (not shown),  $\Delta\eta_y$  and  $U$  are near-zero for shore-break conditions ( $H_{br}/\gamma < h_{bar}$ ), increase as the water depth at breaking exceeds the height on the bar ( $H_{br}/\gamma > h_{bar}$ ), and saturate at values (equations (7) and (8)) set by the alongshore bathymetric variability ( $\Delta h$ ) when waves start to break in the channel ( $H_{br}/\gamma > h_{chan}$ ).

The dependence of  $\Delta\eta_y$  and  $U$  on wave angle was tested for a set of idealized simulations with fixed wave height ( $H = 0.75$  m), tidal elevation (0.5 m depth on bar crest), channel depth (1.0 m relative to bar crest), and a range of incident wave directions (Figure 10). The parameterized and modeled  $\Delta\eta_y$  is reduced only weakly with increasing wave angle (equation (4)) (Figure 10a), both as a result of the  $\cos^2 \theta_{br}$  dependence of the  $x$  component of wave-breaking accelerations (equation (3)) and as a result of the shoaling and refraction-related reduction in  $H_{br}$  (by up to  $\sim 10\%$ ) for increasing offshore  $\theta$ . This small reduction in  $\Delta\eta_y$  (Figure 10a) leads to a small reduction in  $U$  (equation (5)), whereas the increase in the speed of the alongshore current relative to the size of sea-level tilts (Figure 10b,  $x$  axis) leads to a substantial reduction in the value of  $U$  (Figure 10b,  $y$  axis). Agreement between the simulations and the parameterization is improved if the sensitivity to the ratio  $a = V_A/\sqrt{2g\Delta\eta_y}$  is reduced by half ( $\beta = 0.5$  in equation (6)) (dashed curve in Figure 10b). The nonmonotonic behavior of the simulated  $U$  suggests that under some conditions the

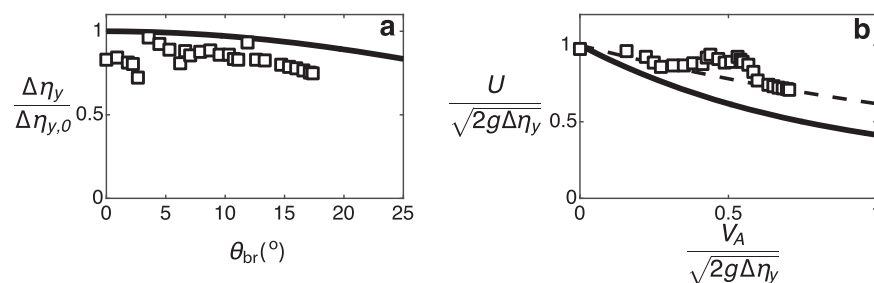


**Figure 10.** (a) Alongshore sea-level difference  $\Delta\eta_y$  normalized by the parameterized sea-level difference for shore normal waves  $\Delta\eta_{y,0}$  versus the wave angle (relative to shore normal) at breaking for model simulations (squares) and a parameterization (curve, equation (4)). (b) Offshore-directed flow speed  $U$  versus alongshore-flow speed  $V_A$  (both axes normalized by  $\sqrt{2g\Delta\eta_y}$ , the parameterized speed of flows driven by a sea-level difference  $\Delta\eta_y$ ) for the simulations (squares) and a parameterization (solid curve, equations (5) and (6)). Dashed curve is the parameterization with the sensitivity to the ratio  $a = V_A/\sqrt{2g\Delta\eta_y}$  reduced by half. The simulations have a range of wave angles and fixed wave height, bathymetry, and tidal elevation.

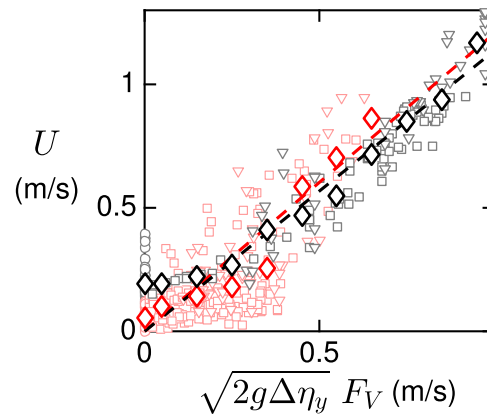


**Figure 11.** Observed (light red symbols) and simulated (light gray symbols)  $U$  versus the parameterized offshore-directed flow speed  $\sqrt{2g\Delta\eta_y} F_V$  (equation (5)). The symbol shape indicates whether the wave-breaking pattern is shore-break (circles), bar-break (squares), or saturated (triangles). The observations ( $r^2 = 0.6$ ) and simulations ( $r^2 = 0.9$ ) are correlated with the parameterization. Least squares fits (constrained to go through the origin) of binned observations (red diamonds) and simulations (black diamonds) to  $\sqrt{2g\Delta\eta_y} F_V$  have slopes of 1.2 (dashed red line) and 1.1 (dashed black line), respectively. The bins are 0.1 m wide, centered every 0.05 m/s, with an additional bin for  $x$  axis values equal to 0.

alongshore flow may enhance (rather than suppress) the offshore-directed flow [Aagaard et al., 1997; Haller et al., 2002; Kumar et al., 2011].

Observed and modeled offshore-directed flow speeds are correlated with the parameterized speed (Figure 11) for simulations with a range of tidal elevations ( $h_{bar} = 0.2\text{--}2.0$  m), wave heights ( $H = 0.05\text{--}2.00$  m), wave angles ( $\theta = 0^\circ\text{--}45^\circ$ ), and idealized channel depths ( $\Delta h = 0.1\text{--}1.0$  m) incising a 1 m high bar. Observations when the channel was nearly filled ( $\Delta h < 0.2$  m) were excluded. Using  $\gamma = \gamma_{BJ} = 0.73$  in the parameterization yields reasonable agreement between the parameterized and modeled  $\Delta\eta_y$  and  $U$  (Figures 9 and 11). However, the correlation between the parameterized and modeled  $U$  increased with  $\gamma$  ( $0.5 < r^2 < 0.9$  for  $0.3 < \gamma < 0.9$ ), whereas the maximum correlation ( $r^2 = 0.6$ ) between the parameterized and observed  $U$  occurs for  $\gamma = 0.5$  ( $r^2 = 0.4, 0.6, 0.5, 0.4$  for  $\gamma = 0.3, 0.5, 0.7, 0.9$ ). Using a smaller  $\gamma$  in the parameterization may compensate for a smaller relevant  $h_{bar}$  when the observed bathymetry is terrace-like, unlike the idealized barred model bathymetry.

Least squares fits of binned from observations (red diamonds in Figure 11) and from simulations (black diamonds in Figure 11) to  $\sqrt{2g\Delta\eta_y} F_V$  have slopes of 1.1 and 1.2, respectively (Figure 11). The slopes are sensitive to bin sizes ( $\sim 15\%$  difference) and to the choice of  $\gamma$  in the parameterization (for  $0.4 < \gamma < 1.0$ , the slopes range from 0.8 to 1.1 and 0.7 to 1.5 for the observations and model results, respectively).

Both the observations and idealized model runs include shore-break (circles, Figure 11), bar-break (squares, Figure 11), and saturated (triangles, Figure 11) conditions. For the conditions of some model runs, the parameterization estimates that waves do not dissipate on the bar, leading to shore-break conditions with no offshore-directed flows, whereas the simulated offshore-directed flows are as high as 0.4 m/s (Figure 11, circles at 0 on the  $x$  axis). Although high tidal elevations are parameterized as “shore-break” conditions, in the simulations with large waves there is wave focusing and enhanced dissipation on the sides of the channel near the shoreline, resulting in alongshore pressure gradients. For bar-break and saturated conditions (squares and triangles in Figure 11), the observed and modeled flows are correlated with the parameterization, but there is significant scatter. The parameter overpredicts the observed  $U$  for parameterized values with  $0.2 < \sqrt{2g\Delta\eta_y} < 0.4$  m/s, usually for cases with large  $\theta$  and  $V_A$ , suggesting that the parameterization may underestimate the suppression of observed cross-shore flows by alongshore flows. Alternatively, the in situ sensors may not have resolved the strongest offshore-directed flows under these conditions (e.g., Figure 5d).

Correlation of the parameter with the observations is weaker if  $F_V$  is excluded (i.e., setting  $F_V = 1$ ) ( $r^2 = 0.5$ ). The correlation for the simulations did not change significantly when excluding  $F_V$  ( $r^2 = 0.9$ ) or

when using  $F_V$  with  $\beta = 1$  (equations (6) and (7)) ( $r^2 = 0.9$ ), although  $F_V$  qualitatively approximates the decrease of simulated  $U$  with increasing alongshore-flow speed (Figure 10b). Previous studies have hypothesized that for small bathymetric perturbations, the effect of the alongshore flow on the offshore-directed flow is a function of a shallow water Reynolds number (ratio of advective to frictional effects) [Wilson *et al.*, 2013; Garnier *et al.*, 2013]. However, for the large bathymetric perturbations here,  $U$  is not suppressed as strongly as predicted by the shallow water Reynolds number theory, and frictional effects are not important relative to the large alongshore pressure-gradient forcing. Instead, for large perturbations, the sensitivity of  $U$  to alongshore flows is a function of  $V_A/\sqrt{2g\Delta\eta_y}$ , related to the relative importance of advective effects (inertia) associated with an alongshore flow and pressure-gradients resulting from nonuniform bathymetry.

## 5. Conclusions

Waves, currents, and bathymetry were observed in and near initially 0.5–2.0 m deep channels dredged across the surf zone. Observed 1 h mean circulation patterns included several days with a strong (up to 1 m/s) rip-current jet with converging feeder currents and several cases with smaller rip currents. A majority of the observed circulation patterns included meandering alongshore currents with offshore-directed flows at the downstream edge of the channel.

The numerical model COAWST reproduced the observed flow patterns, including meandering alongshore currents, converging feeder currents, and tidally modulated rip currents for a range of observed wave conditions and bathymetries, with observed bathymetry near the dredged channel and alongshore uniform bathymetry elsewhere in the domain. The model-data agreement suggests that the circulation observed near the deep channels was controlled primarily by the local channel bathymetry, rather than by nonuniform offshore bathymetry. However, the measured and modeled positions of the strongest offshore-directed flows, feeder currents, and alongshore flow meanders often differed.

Breaking-wave-driven setup patterns on nonuniform bathymetry drove the modeled rip-current circulation patterns and spatial accelerations of alongshore flows. Pressure gradients and wave-breaking accelerations were balanced by the sum of advective accelerations and the vortex force, similar to previous numerical and laboratory results with idealized bathymetry and waves. Although the balances were similar for a range of conditions, their spatial structure was sensitive to the irregular bathymetry and wave conditions. Pressure gradients resulting from gradients in wave forcing near the deep dredged channels were an order of magnitude larger than bottom stress, in contrast to previous results for obliquely incident waves over small bathymetric variations, in which alongshore pressure gradients resulting from the nonuniform bathymetry are a relatively small perturbation on the balance of wave-breaking accelerations and bottom stress.

Based on the primary balance of pressure gradients and advective accelerations, the maximum offshore-directed flow speed  $U$  was parameterized as  $U \approx \sqrt{2g\Delta\eta_y} F_V$ , where  $\Delta\eta_y$  is the alongshore sea-level difference resulting from wave breaking on the channel bathymetry. The sea-level difference, estimated as a function of the breaking wave height and angle, the water depths in the channel and on the bar, and a criterion for depth-limited wave breaking, is near zero when waves break only near the shoreline ("shore-break"), increases with wave height when waves break on the shallow sides but not in the channel ("bar-break"), and reaches a maximum when waves break offshore of the bathymetric variability ("saturated"). The factor  $F_V$  accounts for the suppression of  $U$  by the presence (inertia) of obliquely incident breaking-wave-driven alongshore flows  $V_A$ , and is a function of the ratio of the speed of the breaking-wave-driven alongshore flow to the speed of pressure gradient-driven flows  $V_A/\sqrt{2g\Delta\eta_y}$ . Observed and modeled offshore-directed flow speeds are correlated with the parameterized speed. Observed transitions between alongshore flows and rip currents are consistent with the parameterized response of  $U$  to the wave angle, with obliquely incident waves producing alongshore flows that lead to weaker offshore-directed flows. In addition, the strong observed tidal modulation of the rip-current speed is consistent with the parameterized transition between shore-break and bar-break conditions as the ratio of wave height to water depth on the bar crest varies between high and low tide.

### Acknowledgments

Data are available via e-mail to the corresponding author. We thank the PVLAB field crew for rapidly deploying a remarkable number of sensors in five surfzone rip channels in difficult conditions, the USACE Field Research Facility for excellent field support, and members of the COAWST user community for assistance with the model development. We thank Tuba Özkan-Haller, Steve Lentz, John Trowbridge, Matthieu de Schipper, and two anonymous reviewers for helpful comments. Support was provided by a National Security Science and Engineering Faculty Fellowship and a Vannevar Bush Fellowship funded by the Office of the Assistant Secretary of Defense for Research and Engineering, NDSEG, ONR, and NSF. Any use of trade, firm, or product names is for descriptive purposes only and does not imply endorsement by the U.S. Government.

### References

- Aagaard, T., B. Greenwood, and J. Nielsen (1997), Mean currents and sediment transport in a rip channel, *Mar. Geol.*, *140*(1-2), 25–45, doi:10.1016/S0025-3227(97)00025-X.
- Apotsos, A., B. Raubenheimer, S. Elgar, R. T. Guza, and J. A. Smith (2007), Effects of wave rollers and bottom stress on wave setup, *J. Geophys. Res.*, *112*, C02003, doi:10.1029/2006JC003549.
- Apotsos, A., B. Raubenheimer, S. Elgar, and R. T. Guza (2008), Testing and calibrating parametric wave transformation models on natural beaches, *Coastal Eng.*, *55*(3), 224–235, doi:10.1016/j.coastaleng.2007.10.002.
- Austin, M., T. Scott, Jeff Brown, Jenna Brown, J. MacMahan, G. Masselink, and P. Russell (2010), Temporal observations of rip-current circulation on a macro-tidal beach, *Cont. Shelf Res.*, *30*, 1149–1165, doi:10.1016/j.csr.2010.03.005.
- Austin, M. J., G. Masselink, T. M. Scott, and P. E. Russell (2014), Water-level controls on macro-tidal rip currents, *Cont. Shelf Res.*, *75*(1), 28–40, doi:10.1016/j.csr.2013.12.004.
- Battjes, J. A., and J. Janssen (1978), Energy loss and setup due to breaking of random waves, in *Proceedings of 16th International Conference on Coastal Engineering*, pp. 569–587, Am. Soc. of Civ. Eng., Hamburg, Germany.
- Battjes, J. A., and M. J. F. Stive (1985), Calibration and verification of a dissipation model for random breaking waves, *J. Geophys. Res.*, *90*(C5), 9159–9167, doi:10.1029/jc090ic05p09159.
- Bellotti, G. (2004), A simplified model of rip currents systems around discontinuous barriers, *Coastal Eng.*, *51*, 323–335, doi:10.1016/j.coastaleng.2004.04.001.
- Bonneton, P., N. Bruneau, B. Castelle, and F. Marche (2010), Large scale vorticity generation due to dissipating waves in the surf zone, *Discrete Continuous Dyn. Syst.*, *13*(4), 729–738, doi:10.3934/dcdsb.2010.13.729.
- Booij, N., R. Ris, and L. H. Holthuijsen (1999), A third-generation wave model for coastal regions: 1. Model description and validation, *J. Geophys. Res.*, *104*(C4), 7649–7666, doi:10.1029/98JC02622.
- Bowen, A. J. (1969), The generation of longshore currents on a plane beach, *J. Mar. Res.*, *27*, 206–215.
- Bowen, A. J., D. L. Inman, and V. P. Simmons (1968), Wave 'set-down' and set-up, *J. Geophys. Res.*, *73*(8), 2569–2577, doi:10.1029/JB073i008p02569.
- Bruneau, N., P. Bonneton, B. Castelle, and R. Pedreros (2011), Modeling rip-current circulations and vorticity in a high-energy mesotidal-macrotidal environment, *J. Geophys. Res.*, *116*, C07026, doi:10.1029/2010JC006693.
- Castelle, B., H. Michallet, V. Marieu, F. Leckler, B. Dubardier, A. Lambert, C. Berni, P. Bonneton, E. Barthélemy, and F. Bouchette (2010), Laboratory experiment on rip-current circulations over a moveable bed: Drifter measurements, *J. Geophys. Res.*, *115*, C12008, doi:10.1029/2010JC006343.
- Castelle, B., T. Scott, R. W. Brander, and R. J. McCarroll (2016), Rip-current types, circulation and hazard, *Earth Sci. Rev.*, *163*, 1–21, doi:10.1016/j.earscirev.2016.09.008.
- Chapman, D. C. (1985), Numerical treatment of cross-shelf open boundaries in a barotropic coastal ocean model, *J. Phys. Oceanogr.*, *15*, 1060–1075.
- Dalrymple, R., J. MacMahan, A. Reniers, and V. Nelko (2011), Rip Currents, *Annu. Rev. Fluid. Mech.*, *43*, 551–581, doi:10.1146/annurev-fluid-122109-160733.
- Dronen, N., H. Karunarathna, J. Fredsoe, B. Sumer, and R. Deigaard (2002), An experimental study of rip channel flow, *Coastal Eng.*, *45*, 223–238, doi:10.1016/S0378-3839(02)00035-2.
- Dusek, G., and H. Seim (2013), A probabilistic rip-current forecast model, *J. Coastal Res.*, *289*, 909–925, doi:10.2112/JCOASTRES-D-12-00118.1.
- Fedderson, F. and J. H. Trowbridge (2005), The effect of wave breaking on surf-zone turbulence and alongshore currents: A modeling study, *J. Phys. Oceanogr.*, *35*(11), 2187–2203, doi:10.1175/jpo2800.1.
- Fedderson, F., R. T. Guza, S. Elgar, and T. H. C. Herbers (1998), Alongshore momentum balances in the nearshore, *J. Geophys. Res.*, *103*(C8), 15,667–15,676, doi:10.1029/98JC01270.
- Fedderson, F., E. L. Gallagher, R. T. Guza, and S. Elgar (2003), The drag coefficient, bottom roughness, and wave breaking in the nearshore, *Coastal Eng.*, *48*, 189–195, doi:10.1016/s0378-3839(03)00026-7.
- Flather, R. A. (1976), A tidal model of the northwest European continental shelf, *Mem. Soc. R. Sci. Liege*, *6*, 141–164.
- Ganju, N. K., and C. R. Sherwood (2010), Effect of roughness formulation on the performance of a coupled wave, hydrodynamic, and sediment transport model, *Ocean Modell.*, *33*(3–4), 299–313, doi:10.1016/j.ocemod.2010.03.003.
- Garnier, R., A. Falqués, D. Calvete, J. Thiebot, and F. Ribas (2013), A mechanism for sandbar straightening by oblique wave incidence, *Geophys. Res. Lett.*, *40*, 2726–2730, doi:10.1002/grl.50464.
- Gorrell, L., B. Raubenheimer, S. Elgar, and R. T. Guza (2011), SWAN predictions of waves observed in shallow water onshore of complex bathymetry, *Coastal Eng.*, *58*(6), 510–516, doi:10.1016/j.coastaleng.2011.01.013.
- Guza, R., E. Thornton, and N. Christensen Jr. (1986), Observations of steady longshore currents in the surf zone, *J. Phys. Oceanogr.*, *16*(11), 1959–1969, doi:10.1175/1520-0485(1986)016<1959:OOSLCL>2.0.CO;2.
- Haas, K. A., and J. C. Warner (2009), Comparing a quasi-3D to a full 3D nearshore circulation model: SHORECIRC and ROMS, *Ocean Modell.*, *26*, 91–103, doi:10.1016/j.ocemod.2008.09.003.
- Haas, K. A., I. A. Svendsen, M. C. Haller, and Q. Zhao (2003), Quasi-three-dimensional modeling of rip-current systems, *J. Geophys. Res.*, *108*(C7), 3217, doi:10.1029/2002JC001355.
- Haidvogel, D. B., H. G. Arango, K. Hedstrom, A. Beckmann, P. Malanotte-Rizzoli, and A. F. Shchepetkin (2000), Model evaluation experiments in the North Atlantic Basin: Simulations in nonlinear terrain-following coordinates, *Dyn. Atmos. Oceans*, *32*(3–4), 239–281, doi:10.1016/s0377-0265(00)00049-x.
- Haidvogel, D., et al. (2008), Ocean forecasting in terrain-following coordinates: Model formulation and skill assessment of the Regional Ocean Modeling System, *J. Comput. Phys.*, *227*(7), 3595–3624, doi:10.1016/j.jcp.2007.06.016.
- Haller, M. C., R. A. Dalrymple, and I. A. Svendsen (2002), Experimental study of nearshore dynamics on a barred beach with rip channels, *J. Geophys. Res.*, *107*(C6), 3061, doi:10.1029/2001JC000955.
- Hansen, J., B. Raubenheimer, J. List, and S. Elgar (2015), Modeled alongshore circulation and force balances onshore of a submarine canyon, *J. Geophys. Res. Oceans*, *120*, 1887–1903, doi:10.1002/2014JC010555.
- Hanson, J. L., H. C. Friebel, and K. K. Hathaway (2009), Coastal wave energy dissipation: Observations and STWAVE-FP performance, in *11th International Workshop on Wave Hindcasting and Forecasting and 2nd Coastal Hazards Symposium*, Halifax, Nova Scotia, Canada.
- Hasselmann, K., et al. (1973), Measurements of wind and wave growth and swell decay during the Joint North Sea Wave Project (JONSWAP), *Dtsch. Hydrogr. Z. Suppl.*, *12*, A8.
- Henderson, S. M., J. S. Allen and P. A. Newberger (2004), Nearshore sandbar migration predicted by an eddy-diffusive boundary layer model, *J. Geophys. Res.*, *109*, C02064, doi:10.1029/2003JC002137.

- Houser, C., R. Arnott, S. Ulzhöfer, and G. Barrett (2013), Nearshore circulation over transverse bar and rip morphology with oblique wave forcing, *Earth Surf. Processes Landforms*, *38*(11), 1269–1279, doi:10.1002/esp.3413.
- Kennedy, A., Y. Zhang, and K. Haas (2008), Rip-currents with varying gap widths, *J. Waterw. Port Coastal Ocean Eng.*, 61–65, doi:10.1061/(ASCE)0733-950X(2008)134:1(61).
- Kuik, A., G. van Vledder, and L. Holthuijsen (1988), A method for the routine analysis of pitch-and-roll buoy wave data, *J. Phys. Oceanogr.*, *18*, 1020–1034.
- Kumar, N., G. Voulgaris, and J. C. Warner (2011), Implementation and modification of a three-dimensional radiation stress formulation for surf zone and rip-current applications, *Coastal Eng.*, *58*(12), 1097–1117, doi:10.1016/j.coastaleng.2011.06.009.
- Kumar, N., G. Voulgaris, J. C. Warner, and M. Olabarrieta (2012), Implementation of the vortex force formalism in the coupled ocean-atmosphere-wave-sediment transport (COAWST) modeling system for inner shelf and surf zone applications, *Ocean Modell.*, *47*, 65–95, doi:10.1016/j.ocemod.2012.01.003.
- Kumar, N., F. Feddersen, Y. Uchiyama, J. McWilliams, and W. O'Reilly (2015), Mid-shelf to surfzone coupled ROMS-SWAN model data comparison of waves, currents, and temperature: Diagnosis of subtidal forcings and response, *J. Phys. Oceanogr.*, *45*(6), 1464–1490, doi:10.1175/JPO-D-14-0151.1.
- Lentz, S., and B. Raubenheimer (1999), Field observations of wave setup, *J. Geophys. Res.*, *104*(C11), 25,867–25,875, doi:10.1029/1999JC900239.
- Lentz, S., R. T. Guza, S. Elgar, F. Feddersen, and T. Herbers (1999), Momentum balances on the North Carolina inner shelf, *J. Geophys. Res.*, *104*(C8), 18,205–18,226.
- List, J. H., L. Benedet, D. M. Hanes, and P. Ruggiero (2009), Understanding differences between Delft3D and empirical predictions of alongshore sediment transport gradients, in *Proceedings of 31th International Conference on Coastal Engineering*, pp. 1864–1875, World Sci., Singapore.
- Long, J. W., and H. T. Özkan-Haller (2005), Offshore controls on nearshore rip currents, *J. Geophys. Res.*, *110*, C12007, doi:10.1029/2005JC003018.
- Long, J. W., and H. T. Özkan-Haller (2016), Forcing and variability of nonstationary rip currents, *J. Geophys. Res. Oceans*, *121*, 520–539, doi:10.1002/2015JC010990.
- Longuet-Higgins, M. S. (1970), Longshore currents generated by obliquely incident sea waves, 1, *J. Geophys. Res.*, *75*(33), 6778–6789, doi:10.1029/jc075i033p06778.
- Longuet-Higgins, M. S., and R. W. Stewart (1964), Radiation stresses in water waves; a physical discussion, with applications, *Deep Sea Res. Oceanogr. Abstr.*, *11*(4), 529–562, doi:10.1016/0011-7471(64)90001-4.
- MacMahan, J. H., E. B. Thornton, T. P. Stanton, and A. J. H. M. Reniers (2005), RIPEX: Observations of a rip-current system, *Mar. Geol.*, *218*(1–4), 113–134, doi:10.1016/j.margeo.2005.03.019.
- MacMahan, J. H., E. B. Thornton, and A. J. H. M. Reniers (2006), Rip-current review, *Coastal Eng.*, *53*(2–3), 191–208, doi:10.1016/j.coastaleng.2005.10.009.
- MacMahan, J., et al. (2010), Mean Lagrangian flow behavior on an open coast rip-channeled beach: A new perspective, *Mar. Geol.*, *268*(1–4), 1–15, doi:10.1016/j.margeo.2009.09.011.
- McCarroll, R. J., R. W. Brander, I. L. Turner, H. E. Power, and T. R. Mortlock (2014), Lagrangian observations of circulation on an embayed beach with headland rip currents, *Mar. Geol.*, *355*, 173–188, doi:10.1016/j.margeo.2014.05.020.
- McWilliams, J. C., J. M. Restrepo, and E. M. Lane (2004), An asymptotic theory for the interaction of waves and currents in coastal waters, *J. Fluid Mech.*, *511*, 135–178, doi:10.1017/s0022112004009358.
- Moulton, M., S. Elgar, and B. Raubenheimer (2014), Improving the time resolution of surfzone bathymetry using *in situ* altimeters, *Ocean Dyn.*, *64*(5), 755–770, doi:10.1007/s10236-014-0715-8.
- Mulligan, R. P., A. E. Hay, and A. J. Bowen (2010), A wave-driven jet over a rocky shoal, *J. Geophys. Res.*, *115*, C10038, doi:10.1029/2009JC006027.
- Olabarrieta, M., W. R. Geyer, and N. Kumar (2014), The role of morphology and wave-current interaction at tidal inlets: An idealized modeling analysis, *J. Geophys. Res. Oceans*, *119*, 8818–8837, doi:10.1002/2014JC010191.
- Pitman, S., S. L. Gallop, I. D. Haigh, G. Masselink, and R. Ranasinghe (2016), Wave breaking patterns control rip-current flow regimes and surfzone retention, *Mar. Geol.*, *382*, 176–190, doi:10.1016/j.margeo.2016.10.016.
- Putrevu, U., J. Oltman-Shay, and I. A. Svendsen (1995), Effect of alongshore nonuniformities on longshore current predictions, *J. Geophys. Res.*, *100*(C8), 16,119–16,130.
- Raubenheimer, B., R. T. Guza, and S. Elgar (1996), Wave transformation across the inner surf zone, *J. Geophys. Res.*, *101*(C11), 25,589–25,597, doi:10.1029/96JC02433.
- Raubenheimer, B., S. Elgar, and R. T. Guza (2001), Field observations of wave-driven setdown and setup, *J. Geophys. Res.*, *106*(C3), 4629–4638, doi:10.1029/2000JC000572.
- Reniers, A. J. H. M., E. B. Thornton, and J. A. Roelvink (2004), Morphodynamic modeling of an embayed beach under wave-group forcing, *J. Geophys. Res.*, *109*, C01030, doi:10.1029/2002JC001586.
- Sancho, F. (1998), Unsteady nearshore currents on longshore varying topographies, PhD thesis, Cent. for Appl. Coastal Res., Univ. of Del., Newark, Del.
- Shchepetkin, A. F., and J. C. McWilliams (2005), The Regional Ocean Modeling System (ROMS): A split-explicit, free-surface, topography-following-coordinate ocean model, *Ocean Modell.*, *9*, 347–404, doi:10.1016/j.ocemod.2004.08.002.
- Shchepetkin, A. F., and J. C. McWilliams (2009), Correction and commentary for "Ocean forecasting in terrain-following coordinates: Formulation and skill assessment of the Regional Ocean Modeling System" by Haidvogel et al., *J. Comput. Phys.*, *227*, 3595–3624. *J. Comput. Phys.*, *228*, 8985–9000, doi:10.1016/j.jcp.2009.09.002.
- Slinn, D. N., J. S. Allen, and R. A. Holman (2000), Alongshore currents over variable beach topography, *J. Geophys. Res.*, *105*(C7), 16,971–16,998, doi:10.1029/2000JC900051.
- Smith, J. A. (2006), Wave-current interactions in finite depth, *J. Phys. Oceanogr.*, *36*, 1403–1419, doi:10.1175/JPO2911.1.
- Sonu, C. J. (1972), Field observation of nearshore circulation and meandering currents, *J. Geophys. Res.*, *77*(18), 3232–3247, doi:10.1029/JC077i018p03232.
- Svendsen, I. A., K. A. Haas, and Q. Zhao (2000), Analysis of rip-current systems, in *Proceedings of 27th Coastal Engineering Conference*, pp. 1127–1140, Am. Soc. of Civ. Eng., Sydney.
- Tajima, Y., and O. S. Madsen (2006), Modeling near-shore waves, surface rollers and undertow velocity profiles, *J. Waterw. Port Coastal Ocean Eng.*, *132*(6), 429–438, doi:10.1061/ASCE0733-950X2006132:6429.
- Thornton, E. B. (1970), Variation of longshore current across the surfzone, in *Proceedings of 12th International Conference on Coastal Engineering*, pp. 291–308, New York.
- Thornton, E. B., and R. T. Guza (1983), Transformation of wave height distribution, *J. Geophys. Res.*, *88*(C10), 5925–5938.
- Thornton, E. B., and R. T. Guza (1986), Surf zone longshore currents and random waves: Field data and models, *J. Phys. Oceanogr.*, *16*, 1165–1178, doi:10.1175/1520-0485(1986)016<1165:SZLCAR>2.0.CO;2.

- Uchiyama, Y., J. C. McWilliams, and A. F. Shchepetkin (2010), Wave–current interaction in an oceanic circulation model with a vortex-force formalism: Application to the surf zone, *Ocean Modell.*, *34*(1–2), 16–35, doi:10.1016/j.ocemod.2010.04.002.
- van der Westhuysen, A. J. (2010), Modeling of depth-induced wave breaking under finite depth wave growth conditions, *J. Geophys. Res.*, *115*, C01008, doi:10.1029/2009JC005433.
- Voulgaris, G., N. Kumar, and J. C. Warner (2011), Methodology for prediction of rip currents using a Three-Dimensional numerical, coupled, wave current model, in *Rip Currents: Beach Safety, Physical Oceanography, and Wave Modeling*, edited by S. Leatherman and J. Flettemeyer, CRC Press, Boca Raton, Fla.
- Warner, J. C., C. R. Sherwood, H. G. Arango, R. P. Signell, and B. Butman (2005), Performance of four turbulence closure models implemented using a generic length scale method, *Ocean Modell.*, *8*, 81–113.
- Warner, J. C., C. R. Sherwood, R. P. Signell, C. K. Harris, and H. G. Arango (2008), Development of a three-dimensional, regional, coupled wave, current, and sediment-transport model, *Comput. Geosci.*, *34*(10), 1284–1306, doi:10.1016/j.cageo.2008.02.012.
- Warner, J. C., B. Armstrong, R. He, and J. B. Zambon (2010), Development of a Coupled Ocean-Atmosphere-Wave-Sediment Transport (COAWST) modeling system, *Ocean Modell.*, *35*(3), 230–244, doi:10.1016/j.ocemod.2010.07.010.
- Wilson, G. W., H. T. Özkan-Haller, and R. A. Holman (2013), Quantifying the length-scale dependence of surf zone advection, *J. Geophys. Res. Oceans*, *118*, 2393–2407, doi:10.1002/jgrc.20190.
- Winter, G. (2012), Rip-current characteristics at the Dutch Coast: Egmond aan Zee, MSc thesis, TU Delft, Netherlands.
- Winter, G., A. R. van Dongeren, M. A. de Schipper, and J. S. M. van Thiel de Vries (2014), Rip-currents under obliquely incident wind waves and tidal longshore currents, *Coastal Eng.*, *89*, 106–119, doi:10.1016/j.coastaleng.2014.04.001.
- Wu, C. S., and P. Liu (1984), Effects of nonlinear inertial forces on nearshore currents, *Coastal Eng.*, *8*, 15–32, doi:10.1016/0378-3839(84)90020-6.
- Wu, C. S., and P. Liu (1985), Finite element modeling of nonlinear coastal currents, *J. Waterw. Port Coastal Ocean Eng.*, *111*(2), 417–432, doi:10.1061/(ASCE)0733-950X(1985)111:2(417).